

Accepted Manuscript

Numerical study of the hydrodynamics of regular waves breaking over a sloping beach

Pierre Lubin, Stéphane Glockner, Olivier Kimmoun, Hubert Branger

PII: S0997-7546(11)00002-1
DOI: 10.1016/j.euromechflu.2011.01.001
Reference: EJMFLU 2486

To appear in: *European Journal of Mechanics B/Fluids*



Please cite this article as: P. Lubin, S. Glockner, O. Kimmoun, H. Branger, Numerical study of the hydrodynamics of regular waves breaking over a sloping beach, *European Journal of Mechanics B/Fluids* (2011), doi:10.1016/j.euromechflu.2011.01.001

This is a PDF file of an unedited manuscript that has been accepted for publication. As a service to our customers we are providing this early version of the manuscript. The manuscript will undergo copyediting, typesetting, and review of the resulting proof before it is published in its final form. Please note that during the production process errors may be discovered which could affect the content, and all legal disclaimers that apply to the journal pertain.

1
2
3
4
5
6
7
8
9
10
11
12
13
14
15
16
17
18
19
20
21
22
23
24
25
26
27
28
29
30
31
32
33
34
35
36
37
38
39
40
41
42
43
44
45
46
47
48
49
50
51
52
53
54
55
56
57
58
59
60
61
62
63
64
65

Numerical study of the hydrodynamics of regular waves breaking over a sloping beach

Pierre Lubin^{*,a}, Stéphane Glockner^a, Olivier Kimmoun^b, Hubert Branger^c

^a *Université de Bordeaux, IPB, TREFLE UMR CNRS 8508, ENSCBP, 16 avenue Pey-Berland 33607 Pessac Cedex France*

^b *École Centrale de Marseille, Laboratoire de Recherche et Développement (LRD), Technopôle de Château-Gombert, 38 rue Joliot Curie, 13451 MARSEILLE Cedex 20, France*

^c *Aix-Marseille Université, Institut de Recherche sur les Phénomènes Hors Équilibre (IRPHE), UMR CNRS 6594, Technopôle de Château-Gombert, 49 rue Joliot Curie, 13384 Marseille Cedex 13, France*

Abstract

In the last three decades, great improvements have been brought to the knowledge of the hydrodynamics and general processes occurring in the surf zone, widely affected by the breaking of the waves. Nevertheless, the turbulent flow structure is still very complicated to investigate. The aim of this work is to present and discuss the results obtained by simulating two-dimensional breaking waves by solving the Navier-Stokes equations, in air and water, coupled with a dynamic subgrid scale turbulence model (Large Eddy Simulation, LES). First, the ability of the numerical tool to capture the crucial features of this complicated turbulent two-phase flow is demonstrated. Numerical results are compared with experimental observations provided by Kimmoun and Branger [1]. Spilling/plunging breaking regular waves are con-

*Corresponding author. Tel.: +33 (0) 540 003 307, Fax: +33 (0) 540 006 668

Email addresses: lubin@enscbp.fr (Pierre Lubin), glockner@enscbp.fr (Stéphane Glockner), olivier.kimmoun@centrale-marseille.fr (Olivier Kimmoun), branger@irphe.univ-mrs.fr (Hubert Branger)

sidered. Generally, there is good agreement and the model provides a precise and efficient tool for the simulation of the flow field and wave transformations in the nearshore.

Key words: Navier-Stokes, Numerical simulation, Large Eddy Simulation, Two-phase flow, Breaking waves, Splash-up, Air entrainment, Vortices

1. Introduction

Simulating the air entrainment phenomenon generated by breaking waves remains a major challenge for modern CFD tools. Numerous problems motivated by fundamental research and applications, from environmental and coastal engineering sciences, require an accurate description of wave breaking. Highly complex hydrodynamic features are usually encountered in the surf zone: transition from irrotational flow motion to high frequency turbulence, interacting with large- and small-scale interface deformations, from overturning and breaking of the waves to complex fractioning and coalescence of bubbles and droplets. A broad range of relevant length and time scales is thus involved in this multiphase turbulent flow, making it extremely complicated to investigate both experimentally and numerically.

The general knowledge and understanding of turbulence generated by breaking waves have greatly been improved in the last three decades. Broken waves involve motions of different types and scales, including large-scale coherent vortical motions and small-scale turbulence [2]. Once waves break, a large amount of energy is released and turned into turbulence [3]. Nevertheless, a lot of work still has to be done, some aspects suffering from a lack of efficiency or unsolved limitations. It is widely accepted that such

1
2
3
4
5
6
7
8
9 complicated high-Reynolds number turbulent multiphase flow is inaccessible
10 for Direct Numerical Simulations (DNS), Reynolds Averaged Navier-Stokes
11 Equations (RANS) or Large Eddy Simulations (LES) therefore being effective
12 alternatives.
13
14
15

16 Zhao and Tanimoto [4] first applied the LES method to breaking waves
17 and showed very promising results compared with experimental measure-
18 ments, considering a two-dimensional configuration. Then some numerical
19 works proved the ability of the LES method [5, 6, 7, 8, 9] to deal with spilling,
20 plunging, strongly plunging and spilling/plunging breakers. The authors pro-
21 vided a great improvement in the numerical methods allowing a description
22 with a very promising accuracy for both the free surface and the general be-
23 havior of the turbulent flow structures. Major contributions gave interesting
24 insights into the hydrodynamics under broken waves. Nevertheless, as all the
25 cited authors stated, air entrainment was not taken into account, although it
26 was widely identified as an important feature to be considered. Indeed, most
27 numerical surf zone studies are based on single phase flow assumption, ignor-
28 ing the air phase for the convenience of computation. Moreover, comparisons
29 led to the conclusion that the poor description of air/water mixing was re-
30 sponsible for the discrepancies observed due to coarse mesh grid resolutions.
31 Strong surface distortions, surface tension and air-water interactions were
32 usually omitted. A generally good agreement was usually found, but some
33 major differences were shown to occur when phase-averaged velocity and tur-
34 bulent quantities were examined in aerated regions. Indeed, the resolution
35 was mainly chosen to provide acceptable computation times with a sufficient
36 accuracy for the free surface description considering the macro structures.
37
38
39
40
41
42
43
44
45
46
47
48
49
50
51
52
53
54
55
56
57
58
59
60
61
62
63
64
65

1
2
3
4
5
6
7
8
9 This often resulted in missing the correct breaking point, which is very sen-
10 sitive to any imperfections in wave generation [9]. It was also found that the
11 results of plunging breakers showed better agreement than spilling breakers
12 compared to experimental measurements.
13
14
15

16 Many experimental works drew attention to the generation and the im-
17 portance of air entrainment during the wave breaking process [10, 11, 2, 12,
18 13, 14]. The velocity field under broken waves is characterized by the ex-
19 istence of very active turbulence associated with air entrainment, which is
20 responsible for wave energy damping in the surf zone. Lin and Hwung [15]
21 showed that the main mechanism driving the motion in the bubble region
22 was the vortex system generated during the jet-splash cycles. Experiments
23 proved that the eddies contained a large quantity of air bubbles which en-
24 hanced the upwelling of sediment. Chanson and Lee [16] measured the rate of
25 energy dissipation to be increased with the bubble penetration depth. Huang
26 et al. [17] recently presented experimental measurements of spilling break-
27 ing waves. Significant turbulent dissipation was shown to occur initially in
28 the roller region at the frontal wave crest and then to spread to the entire
29 crest region after the establishment of a turbulent bore. The small-scale
30 interactions thus have important effects on large-scale behavior [18].
31
32
33
34
35
36
37
38
39
40
41
42
43
44

45 More recent numerical studies proved the importance of air entrainment
46 for turbulence generation in numerical simulations of breaking waves. Chris-
47 tensen et al. [19] highlighted that since the mixture of air and water in the
48 roller region had, on average, a smaller density than that of the water, the
49 turbulence produced in the roller would have difficulties in penetrating the
50 underlying fluid. Therefore, a large part of the production and dissipation
51
52
53
54
55
56
57
58
59
60
61
62
63
64
65

1
2
3
4
5
6
7
8
9 took place in the roller before it was diffused downward, which explained the
10 overestimation on the turbulence in the surf zone by numerical models so
11 far. Moreover, the de-entrainment of air bubbles from the water after wave
12 breaking may have released some wave energies into the air and may have
13 contributed significantly to the wave energy dissipation process. Hieu and
14 Tanimoto [20] improved their numerical model [6] showing better compar-
15 isons with experimental data concerning free surface elevations. The numer-
16 ical results were also compared with those from Zhao et al. [7] and a higher
17 accuracy was shown. They pointed out the major role of air entrainment and
18 the necessity to take it into account to get accurate numerical results. Lubin
19 et al. [21] discussed the results obtained from simulating three-dimensional
20 plunging breaking waves by solving the Navier-Stokes equations, in air and
21 water. The splash-up mechanism was carefully detailed and vortex genera-
22 tion and air entrainment processes were described. The behavior of the gas
23 pockets was analyzed and its impact on energy dissipation was shown. Re-
24 cently, Wang et al. [22, 23] improved the numerical methods for describing
25 the free surface, dedicated to breaking waves. Iafrati [24] numerically ana-
26 lyzed the role played by the breaking intensity on free surface dynamics, air
27 entrainment and general hydrodynamics. Clear improvements were made to
28 the general understanding of the complicated flow.

29
30
31
32
33
34
35
36
37
38
39
40
41
42
43
44
45
46
47 Kimmoun and Branger [1] recently experimented surf-zone breaking waves.
48 Particle Image Velocimetry (PIV) experimental techniques were improved to
49 be able to calculate velocities and void fractions in the aerated regions. De-
50 tailed pictures showed that a short spilling event occurred at the crest of the
51 waves, before degenerating into strongly plunging breaker. Numerical works
52
53
54
55
56
57
58
59
60
61
62
63
64
65

1
2
3
4
5
6
7
8
9 usually showed better agreements when simulating plunging breaking waves
10 than the spilling case compared with available experimental data. Fine mesh
11 grid resolutions and appropriate numerical methods are required to accu-
12 rately describe the length scales of the interface deformations experimentally
13 measured (plunging jet, white foam, etc.).
14
15

16
17
18 Based on a previous numerical study, Lubin et al. [25] presented the re-
19 sults obtained for the LES of 2D and 3D regular waves shoaling and breaking
20 over a sloping beach, compared with the experimental results of Kimmoun et
21 al. [26]. A spilling/plunging breaking event was expected to occur according
22 to the experimental measurements, but the numerical results showed dis-
23 crepancies, due to the coarse mesh grid resolution. So, considering the new
24 experimental results from Kimmoun and Branger [1] and the discrepancies
25 highlighted by Lubin et al. [25], 2D numerical simulation of the phenomenon
26 has been performed to show the ability of the numerical tool to finally cap-
27 ture the spilling initiation process and air entrainment during the early stage
28 of the phenomenon. The effect of air has not been studied yet in detail
29 in most of the cited two- and three-dimensional numerical studies found in
30 the literature. Taking the mixture of air and water into account is crucial
31 and still remains one of the challenges of the coming years. The aim of this
32 paper is to simulate this unsteady two-phase wave breaking motion using a
33 LES method to gain further understanding of the complicated features of
34 the flow, including wave overturning, occurrence of splash-ups and air en-
35 trainment. The limitations in the description of the air entrainment will be
36 highlighted and discussed. Great care will be taken to highlight the impor-
37 tance of the mesh grid size. The paper is organized as follows. In section
38
39
40
41
42
43
44
45
46
47
48
49
50
51
52
53
54
55
56
57
58
59
60
61
62
63
64
65

1
2
3
4
5
6
7
8
9 2, we introduce the numerical model. Numerical wave generation procedure
10 is detailed. Some preliminary numerical results and applications are pro-
11 vided to demonstrate the ability of the numerical tool to deal with breaking
12 waves. We then provide, in section 3, a discussion of the numerical results
13 obtained by simulating regular waves breaking over a sloping beach. This
14 section is devoted to the qualitative comparison of our numerical results with
15 the experimental observations [1]. The case study is carefully described and
16 boundary conditions are given. We aim to accurately describe the free sur-
17 face behavior, as we will focus on capturing and describing the spilling phase
18 experimented by Kimmoun and Branger [1]. Finally, in section 4, a short cri-
19 tique of our numerical results is discussed. We then outline the perspectives
20 and future works.
21
22
23
24
25
26
27
28
29
30
31

32 **2. Description of the numerical model and validation**

33
34
35
36 We solve the Navier-Stokes equations in air and water, coupled with a
37 subgrid scale turbulence model (LES). The numerical tool is well suited to
38 dealing with strong interface deformations occurring during wave breaking,
39 for example, and with turbulence modeling in the presence of a free surface
40 in a more general way. Solving the Navier-Stokes equations in an air/water
41 configuration is still a real challenge, especially when dealing with strong
42 interface deformations and tearing, turbulence and free surface interactions.
43
44
45
46
47
48
49

50 *2.1. Governing equations*

51
52 An incompressible multiphase phase flow between non-miscible fluids can
53 be described by the Navier-Stokes equations in their multiphase form. In the
54 single fluid formulation of the problem [27], a phase function C , or "color"
55
56
57
58
59
60
61
62
63
64
65

function, is used to locate the different fluids standing $C = 0$ in the outer medium, $C = 1$ in the considered medium. Intermediate values of C indicate the proportion of the medium (water) in the control volume around each node of the mesh. The interface between two media is repaired by the discontinuity of C between 0 and 1. In practice, $C = 0.5$ is used to characterize this surface. The governing equations for the Large Eddy Simulation (LES) of an incompressible fluid flow are classically derived by applying a convolution filter to the unsteady Navier-Stokes equations. The resulting set of equations reads (Eqs. 1-3):

$$\nabla \cdot \mathbf{u} = 0 \quad (1)$$

$$\rho \left(\frac{\partial \mathbf{u}}{\partial t} + \mathbf{u} \cdot \nabla \mathbf{u} \right) = -\nabla p + \rho \mathbf{g} + \nabla \cdot (\mu + \mu_t) [\nabla \mathbf{u} + \nabla^T \mathbf{u}] + \mathbf{F} \quad (2)$$

and

$$\frac{\partial C}{\partial t} + \mathbf{u} \cdot \nabla C = 0 \quad (3)$$

where \mathbf{u} is the velocity, C the phase function, t the time, p the pressure, \mathbf{g} the gravity vector, ρ the density, μ the dynamic viscosity, μ_t the turbulent viscosity and \mathbf{F} the surface tension volume force.

To deal with solid obstacles within the numerical domain, it is possible to use multi-bloc domains, but it is often much simpler to consider the numerical domain as a unique porous medium [28, 29, 30]. The permeability coefficient K defines the ability of a porous medium to let pass the fluids more or less freely through it. If this permeability coefficient is large ($K \rightarrow +\infty$), the

medium is equivalent to a fluid. If it is zero, we can model an impermeable solid. A real porous medium is modeled with intermediate values of K . To take this coefficient K into account in our system of equations, we thus add an extra term in the right-hand side of the momentum equations (Eq. 2), $-\frac{\mu}{K}\mathbf{u}$.

The magnitudes of the physical characteristics of the fluids depend on the local phase. They are defined according to C in a continuous manner as:

$$\begin{aligned}\rho &= C\rho_1 + (1 - C)\rho_0 \\ \mu &= C\mu_1 + (1 - C)\mu_0\end{aligned}\quad (4)$$

where ρ_0 , ρ_1 , μ_0 and μ_1 are the densities and viscosities of fluid 0 and 1 respectively.

Based on the review of Lubin and Caltagirone [31], we find that the most widely used subgrid scale model is the Smagorinsky model. However, it has been proved to be much too dissipative [32]. In spite of its negative aspects, its simplicity is still widely appreciated. In Eq. 2), the turbulent viscosity μ_t is calculated with the Mixed Scale model [32], which has proved its accuracy for geophysical flows [33, 34, 21, 35, 36]. The model exhibits a triple dependency on the large and small structures of the resolved field as a function of the cut-off length. The eddy viscosity μ_t is calculated as follows (Eq. 5):

$$\mu_t(\mathbf{x}, t) = \rho C_M \bar{\Delta}^{1+\alpha} (|\bar{S}|)^{\frac{\alpha}{2}} (q_c^2(\mathbf{x}, t))^{\frac{1-\alpha}{2}} \quad (5)$$

where \bar{S} is the resolved deformation rate tensor and $\bar{\Delta}$ is the cut-off length of the filter. C_M is the model constant chosen as $C_M = 0.06$, α is a parameter

with a value that varies between 0 and 1. Generally, and in the following, α is taken to be equal to 0.5. The quantity q_c represents the kinetic energy of the test field extracted from the resolved velocity field through the application of a test filter associated to the cut-off lengthscale $\tilde{\Delta} > \bar{\Delta}$. We choose $\tilde{\Delta} = 2\bar{\Delta}$, because it is the value which is most used and seems to give the best results. This subgrid kinetic energy is assumed to be equal to the kinetic energy at cut-off q_c^2 , evaluated in real space as (Eq. 6):

$$q_c^2(\mathbf{x}, t) = \frac{1}{2} \mathbf{u}(\mathbf{x}, t)' \mathbf{u}(\mathbf{x}, t)' \quad (6)$$

where the *test field* velocity (\mathbf{u}') can be evaluated thanks to an explicit test filter applied to the resolved scales, noted $(\tilde{\cdot})$. This explicit discrete filtering operation is a linear combination of the neighboring values [32, 37]. This test field velocity represents the high frequency part of the resolved velocity field. The use of this model does not require a complementary wall model, as the Smagorinsky model does, because the eddy viscosity vanishes as the kinetic energy tends to zero at cut-off.

Model (Eqs. 1-4) describes all the hydrodynamic and geometrical processes involved in the motion of multiphase media.

2.2. Numerical methods

Time discretization is implicit and the equations are discretized on a staggered grid by means of the finite volume method. A dual grid, or underlying grid [38], is used to gain improved accuracy for the interface description, the mesh grid size being divided by two in each direction for interface tracking. This technique also avoids the interpolations of the physical characteristics

1
2
3
4
5
6
7
8
9 on the staggered grids, since the color function is defined on each point where
10 viscosities and densities are needed.
11

12
13 The main difficulty concerning the numerical treatment of the Navier-
14 Stokes equations (Eqs. 1-2) is the coupling between pressure and velocity
15 and the fulfillment of the incompressibility condition. Following the work
16 of Fortin and Glowinski [39], the Navier-Stokes system is formulated as a
17 velocity / pressure minimization - maximization problem requiring the com-
18 putation of a saddle point (\mathbf{u}, \mathbf{p}) associated with the augmented Lagrangian
19 of the problem. The pressure is considered as a Lagrange multiplier and
20 the incompressibility constraint is introduced implicitly into the momentum
21 equations (Eqs. 2). Then, the saddle-point (\mathbf{u}, \mathbf{p}) is computed using an itera-
22 tive Uzawa algorithm [40]. Parameters of the augmented Lagrangian method
23 are calculated automatically according to the fluids and flow characteristics
24 following [41]. The space derivatives of the inertial term are discretized by a
25 hybrid Upwind-Centered scheme [42] and the viscous term is approximated
26 by a second order centered scheme. The MUMPS direct solver is used to
27 solve the linear systems [43, 44].
28
29
30
31
32
33
34
35
36
37
38
39
40
41

42 Interface tracking is achieved by a Volume Of Fluid method (VOF), which
43 is able to handle interface reconnections without interface reconstruction.
44
45 Lin and Liu [45] gave a complete overview and discussion of the different
46 numerical techniques that have been used for interface tracking in numerical
47 simulations of breaking waves. Given that Eq. 3 is hyperbolic and C is
48 discontinuous, the explicit Total Variation Decreasing (TVD) Lax-Wendroff
49 (LW) scheme of LeVeque [46] is used to directly solve the interface evolutions
50 without the reconstruction of C . When the small scale structures of interface
51
52
53
54
55
56
57
58
59
60
61
62
63
64
65

1
2
3
4
5
6
7
8
9 are large compared with the grid size, the LW-TVD method is accurate
10 and involves controlled numerical diffusion across the interface on three grid
11 points.
12
13

14 The numerical code has already been extensively verified and validated
15 through numerous test cases including mesh refinement analysis [33, 47, 21,
16 36]. The accuracy of the numerical schemes and the conservation laws of
17 mass and energy in the computational domain have been accurately verified.
18 For more details, the numerical methods have already been fully described
19 in Lubin et al. [21].
20
21
22
23
24
25
26

27 *2.3. Internal wave maker*

28
29 Prior to the simulation of the laboratory tests, an effort has been made
30 to implement and validate the procedure of regular and irregular wave gener-
31 ation developed by Lin and Liu [48]. The method consists in introducing an
32 internal mass source function in the continuity equation (Eq. 1) for a chosen
33 group of cells defining the source region:
34
35
36
37
38
39
40
41
42
43

$$44 \quad \nabla \cdot \mathbf{u} = S(x, y, t) \text{ in } \Omega \quad (7)$$

45 where $S(x, y, t)$ is calculated thanks to any chosen analytical wave solution.
46
47

48 *2.4. Validation: a solitary wave propagating and breaking over a submerged* 49 *obstacle*

50
51 Lubin et al.[21] validated the numerical tool considering some dam-break
52 and rising bubbles configurations. In this section, the propagation and the
53 overturning of a stable solitary wave over a submerged reef, consisting of a
54
55
56
57
58
59
60
61
62
63
64
65

1
2
3
4
5
6
7
8
9 rectangular step-like obstacle, is investigated (Fig. 1). The reference case is
10 taken from the work presented by Yasuda et al. [49]. This test case shows
11 the ability of our numerical model to simulate overturning waves accurately,
12 as we will compare the wave profiles at breaking,
13
14

15
16 The mean water depth is $d = 0.31 \text{ m}$ and the height of the obstacle is
17 $D = 0.263 \text{ m}$. The initial amplitude and celerity are $H = 0.131 \text{ m}$ and
18 $c = 2.072 \text{ m}\cdot\text{s}^{-1}$, respectively. The incident solitary wave is initialized in the
19 numerical domain and the crest of the wave is set at $x = 2 \text{ m}$, the internal
20 wave maker is not used in this test case. The reef face is located at $x = 4 \text{ m}$.
21 The velocity field and the free surface profile are initially calculated with the
22 theoretical third-order solitary wave solution [50, 51]. The numerical domain
23 is 8 m long and 0.6 m high, discretized into 1200×200 nonuniform grids
24 in the x-direction, with $\Delta x_{min} \simeq 4 \cdot 10^{-3} \text{ m}$ in the vicinity of the submerged
25 obstacle. Uniform grid spacing $\Delta z_{min} \simeq 3 \cdot 10^{-3} \text{ m}$ is used. The solitary wave
26 propagates towards the right side of the numerical domain.
27
28

29
30 Yasuda et al. [49] used a fully nonlinear potential theory model to study
31 the internal velocity and acceleration fields and their relationship to breaker
32 type. They verified the accuracy of their numerical model with some ex-
33 perimental data. Four capacitance wave gauges recorded the free surface
34 elevations at different locations in the canal. The first gauge was placed up-
35 stream of the reef face to check the incident waveheight. The second gauge
36 was located above the upstream corner of the reef. The last two gauges
37 measured the free surface at 0.515 m and 1.020 m away from the tip of the
38 obstacle.
39
40

41
42 With respect to the positions of the three last gauges (referred to as
43
44
45
46
47
48
49
50
51
52
53
54
55
56
57
58
59
60
61
62
63
64
65

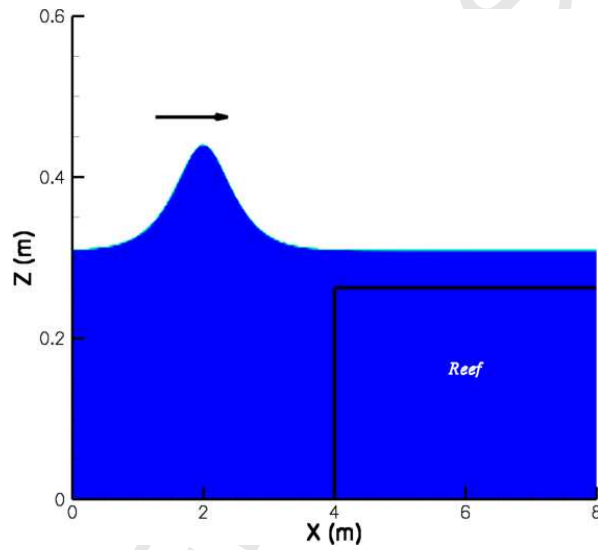


Figure 1: Initial conditions for the propagation and the breaking of a solitary wave over a submerged rectangular reef. $t = 0$ s, $C > 0.5$.

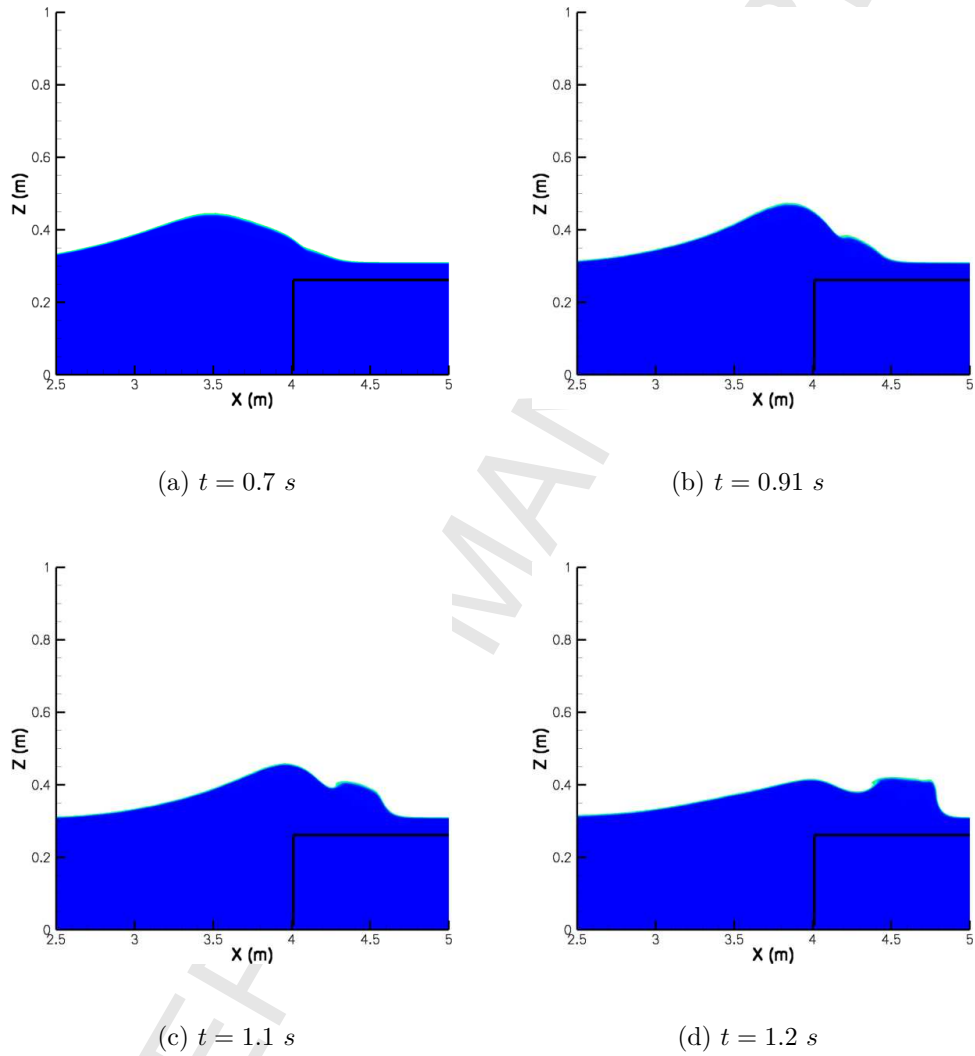


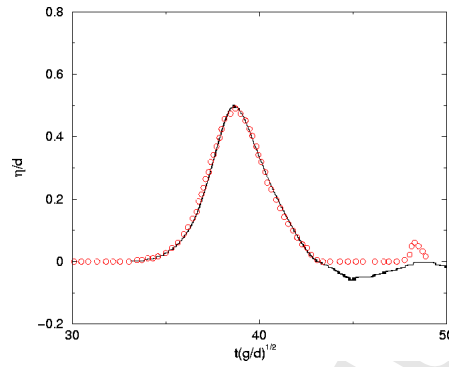
Figure 2: Solitary wave propagating over the submerged reef: initiation of the fission of the wave. The black line represents the reef profile. $C > 0.5$.

Gauges	Numerical	Experimental	Error (%)
P2	0.500	0.505	-1.0
P3	0.348	0.344	1.2
P4	0.358	0.354	1.1

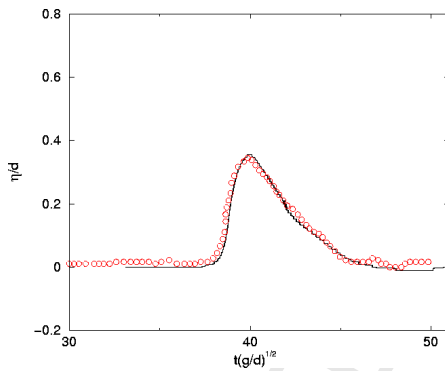
Table 1: Maximum non-dimensional free surface elevation values, η/d , recorded at the three considered locations. Numerical values are compared with the experimental measurements [49].

P2, P3 and P4 by Yasuda et al. [49]), we plot our non-dimensional free surface elevations η/d versus non-dimensional time $t\sqrt{g/d}$, compared with the experimental values (Fig. 3). We can note that our numerical model gives very satisfactory results. The general trend is followed with a reasonable accuracy, the relative errors being presented in Table 1.

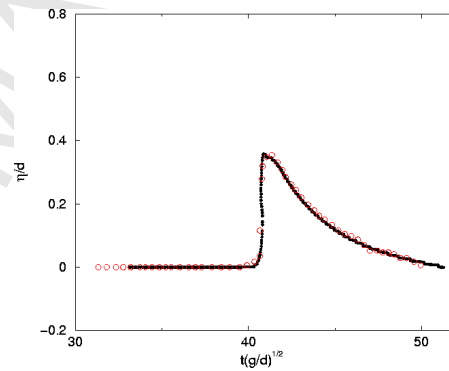
We verify that our numerical model accurately reproduces the propagation and the interaction between the solitary wave and the obstacle. First, the wave propagates over a flat bottom without any change of form, as any stable solitary wave would do. As it reaches the neighborhood of the obstacle, the depth of water over the reef is abruptly reduced, which leads the wave profile being dramatically transformed. The wave is then forced to reorganize itself, causing the fission phenomenon: when solitary waves propagate from deep water into shallower water, the incoming waves disintegrate into two or more solitons [52, 53]. Figs. 2 present the incident wave separating into a solitary wave, going to the left, and a transmitted wave, which is about to break as it goes over the reef towards the right side of the domain. This aspect would have deserved more systematic investigation for validation, but



(a) P2



(b) P3



(c) P4

Figure 3: Comparisons of the non-dimensional free surface elevations, η/d , plotted versus the non-dimensional time, $t\sqrt{g/d}$, recorded at each location P2, P3 and P4. Black line: present numerical results; red \circ : experimental results [49].

1
2
3
4
5
6
7
8
9
10 it is not our concern in this paper.

11 As recorded by the gauge standing over the reef's upstream corner (Fig.
12 3), the free surface elevation rises from the initial non-dimensional value
13 $\eta/d = 0.424$ to $\eta/d = 0.498$. The wave loses symmetry aspect and starts
14 steepening till the front face of the crest becomes vertical (Fig. 4 a). We
15 then have a plunging breaking wave (Fig. 4 b). A jet of liquid is about
16 to be projected from the crest of the wave. It free-falls down forward in a
17 characteristic overturning motion. It was observed that several gas pockets
18 were entrapped.
19
20
21
22
23
24
25

26 In order to compare our results with the work of Yasuda et al. [49],
27 we use the same non-dimensional values. Yasuda's reef face is located at
28 $x/d = 32$, our reef being at $x/d \simeq 12.9$. So, we show in figures (4 (a)
29 and (b)) our free surface profiles translated to the same reference, with η/d
30 the non-dimensional free surface elevation. Figs. (4 a and b) present the
31 non-dimensional free surface profiles of the breaking wave at two different
32 locations. At first glance, the comparisons are not to our advantage, but
33 we voluntary zoomed the graphs, which enlarges the discrepancies. If we
34 consider the abscissa of the vertical front face of the wave (Fig. 4 a), the
35 relative error between our numerical result and the experimental measure-
36 ment is $\simeq -1.5\%$. At the instant of jet fall initiation (Fig. 4 b), if we again
37 consider the abscissa of the vertical face of the wave, under the overhang-
38 ing jet, the relative error between the numerical result and the experimental
39 measurement is $\simeq -1.2\%$. The numerical and experimental jets of water
40 are approximately of the same length. However, we can observe that the
41 computed jet looks "thicker" than the experimental one. This tendency is
42
43
44
45
46
47
48
49
50
51
52
53
54
55
56
57
58
59
60
61
62
63
64
65

generally observed when using VOF methods for simulating breaking waves [54, 33, 22].

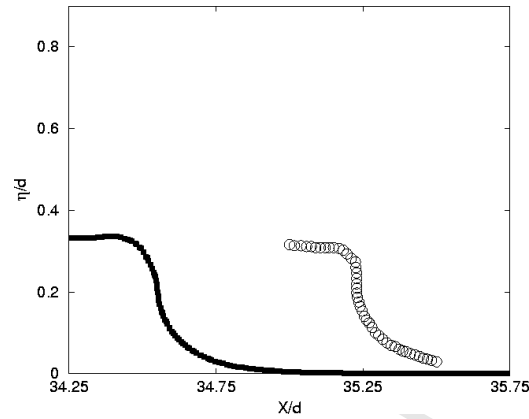
Unfortunately, Yasuda et al. [49] presented no experimental pictures giving information about the abscissa of the jet impact or the splash-up behavior. However, our numerical results fit very well with the published results of Yasuda et al. [49] considering the wave breaking initiation phenomenon. The ability of the numerical tool to predict accurately the breaking point initiation is thus proved.

3. Large Eddy Simulations of breaking waves

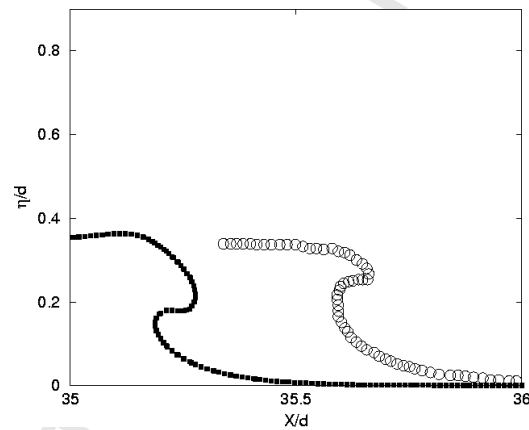
Based on the numerical methods detailed in section 2, Lubin et al. [25] presented the results obtained for the LES of regular 2D and 3D waves shoaling and breaking over a sloping beach, compared with the experimental results from Kimmoun et al. [26]. The main observed differences were that the first short spilling event was missed and the dislocation of the gas pockets into small bubbles could not be simulated, even though, in the numerical results, the gas pockets corresponded to some air-water mixing zones observed in the experimental pictures. In order to overcome the observed discrepancies, mainly due to the coarse mesh grid resolution, new numerical simulation was performed considering the new experimental study from Kimmoun and Branger [1]. The mesh grid distribution was improved to be able to capture the spilling phase.

3.1. Description of the experimental configuration

The experiments were performed in the École Centrale wave tank in Marseille. The glass-windowed tank is 17 m long and 0.65 m wide. The water



(a) Breaking point



(b) Jet fall initiation

Figure 4: Comparison of the free surface profiles (a) prior to the jet ejection and (b) at jet initiation. Black ■: present LES ($C = 0.5$); black ○: experimental results [49]. The variables indicated on both axis are those shown in Figure 4 by Yasuda et al. [49].

1
2
3
4
5
6
7
8
9 depth was set at $d = 0.705 \text{ m}$. The 1/15 sloping beach was about 13 m long,
10 starting at about 4 m from the wavemaker. The length of the surf zone was
11 about 3 m . Camera PIV measurements were made in fourteen different loca-
12 tions from the incipient breaking location up to the swash zone. Fifth order
13 Stokes waves were generated, corresponding to the analytical solution devel-
14 oped by Fenton [55]. The wave period was $T = 1.275 \text{ s}$ and wave amplitude
15 before the sloping beach was $a \simeq 0.057 \text{ m}$. The wavelength was $L \simeq 2.4 \text{ m}$
16 and the measured height at breaking was $H_b = 0.14 \text{ m}$. The waves are ob-
17 served to start breaking about 2.50 m away from the shoreline, or 12.275 m
18 away from the wavemaker.
19
20
21
22
23
24
25
26
27

28 A sketch of a wave breaking event is displayed by Kimmoun and Branger
29 [1]. The wave starts breaking showing a brief spilling phase, the white cap
30 was observed to be about 1 – mm high. Then a jet of liquid is rapidly ejected
31 from the wave crest and the overturning wave front curls forward. A first
32 splash-up is generated when the jet of liquid hits the front face of the wave.
33 We can then see a large amount of air entrained with foam and bubbles.
34 Some other splash-ups are then generated. A roller propagates towards the
35 shoreline, with a great air-water mixing area. It can be seen that the bubbles
36 are generated in the upper part of the water column, and advected towards
37 the bottom with a slight slanting axis. The volume of the entrained bubbles
38 decreases gradually till the wave crosses the shoreline and runs up before
39 coming back. This is in agreement with the general description of Peregrine
40 [56], for example. More details of the experiments are given by Kimmoun
41 and Branger [1].
42
43
44
45
46
47
48
49
50
51
52
53
54
55
56
57
58
59
60
61
62
63
64
65

3.2. Initial and boundary conditions

The computational domain is 15 m long and 1 m high (Fig. 5). The sloping beach starts at $x = 3.5 m$, the source function being located at $x_S = 3.5 m$ and $z_S = 0.3675 m$. The center of the source region is at $d/2$, right above the toe of the sloping beach to save computation time. The numerical beach is considered as an impermeable solid obstacle, the permeability coefficient K being initialized at zero (Eq. 2).

522 000 mesh grid points are used to discretize the numerical domain, with nonuniform grids in both directions ($\Delta x_{min} \simeq 1.10^{-3} m$ and $\Delta z_{min} \simeq 2.5 \times 10^{-3} m$). These values have to be divided by two, in both directions, for the free surface description thanks to the dual grid. Two-phase flow simulations and turbulence modeling require fine mesh cells to be very accurate, even if LES is supposed to save some mesh grid points. Moreover, when simulating two-phase flows, the interface can become smaller than the mesh grid size (droplets or bubbles). These small inclusions are thus “lost” and their contribution to the flow can lead to a wrong description of the flow. In our study, the major physical parameters leading the choice of our mesh grid distribution are the length scales of the free surface deformations, especially the overturning jet and the entrained gas pockets.

The time step is chosen to ensure a Courant-Friedrichs-Levy condition less than 1, necessary for the explicit advection of the free surface. The calculation is made with the densities and the viscosities of air and water ($\rho_a = 1.1768 kg.m^{-3}$ and $\rho_w = 1000 kg.m^{-3}$, $\mu_a = 1.85 \times 10^{-5} kg.m^{-1}.s^{-1}$ and $\mu_w = 1 \times 10^{-3} kg.m^{-1}.s^{-1}$). Table 2 presents the former and new physical and numerical parameters, used in the successive studies.

Experimental studies	Kimmoun et al. [26]	Kimmoun and Branger [1]
$d(m)$	0.735	0.705
$T(s)$	1.3	1.275
$a(m)$	0.07	0.057
$L(m)$	2.5	2.4
$H_b(m)$	0.137	0.14
$x_b(m)$	2.65	2.5
Numerical comparisons	Lubin et al. [25]	Present study
Sizes of domains	$20m \times 1.2m$	$15m \times 1m$
Mesh grid points	520 000	522 000
$\Delta x_{min}(m)$	$5.10^{-3}m$	$\simeq 5.10^{-4}m$
$\Delta z_{min}(m)$	$\simeq 1.25 \times 10^{-3}m$	$\simeq 1.25 \times 10^{-3}m$

Table 2: Physical and numerical parameters used in the successive studies.

The mesh grid sizes have been divided by two considering the dual grid used for the interface capture (see section 2.2).

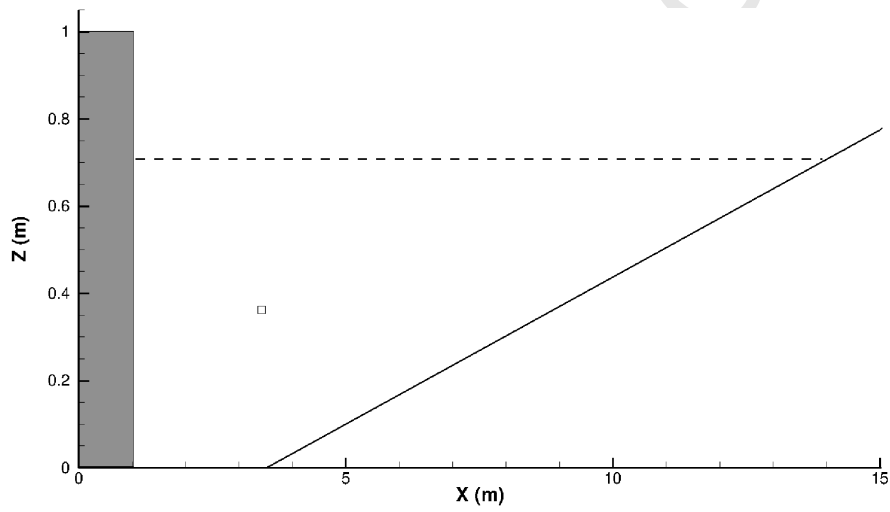


Figure 5: Numerical domain configuration. The small rectangular box is the wave generator, located right above the toe of the sloping beach. The dashed line shows the initial water depth. The gray box on the left side of the numerical domain is a sponge layer. The slanted line shows the sloping beach.

We adapted Fenton's [55] analytical developments for the fifth-order Stokes wave theory, corresponding to the experimental conditions, to the source function method (Eq. 7):

$$S(x, y, t) = \sum_i \sum_j \frac{2c}{Ak} B_{ij} \epsilon^i \cos i \left(\frac{\pi}{2} - \sigma t - p_s \right) \quad (8)$$

where A is the area of the source region. c , k and σ are the celerity, wave number and angular frequency respectively. $\epsilon = \frac{kH}{2}$ is the wave steepness and B_{ij} are dimensionless coefficients. The detailed expressions for the dispersion relationship, wave celerity and B_{ij} coefficients are given by Fenton [55], Sobey et al. [57] or Fenton and McKee [58]. p_s is the phase shift calculated to have $S(x, y, 0) = 0$. The source region is 0.06 m wide and 0.0735 m high. The area and the location of the source function have been designed applying the rules described by Lin and Liu [48]. The height of the source region is recommended to be in the range of $1/10 - 1/2$ of water depth, while the width of the source region is suggested to be less than 5% of the wavelength. The distance between the center of the source region and the still water level is advised to be in the range of $1/3 - 1/2$ of the water depth. The method has been extensively verified and validated compared with analytical profiles to ensure accurate wave generation.

At the beginning of the numerical simulation, the water is at rest, and, as the time increments, the source function is calculated to generate the regular waves. In Fig. 6, we show the velocity field around the source function, acting like a pump. Two trains of surface gravity waves are thus generated, as the free surface responds to a pressure increment defined within the source region cells.

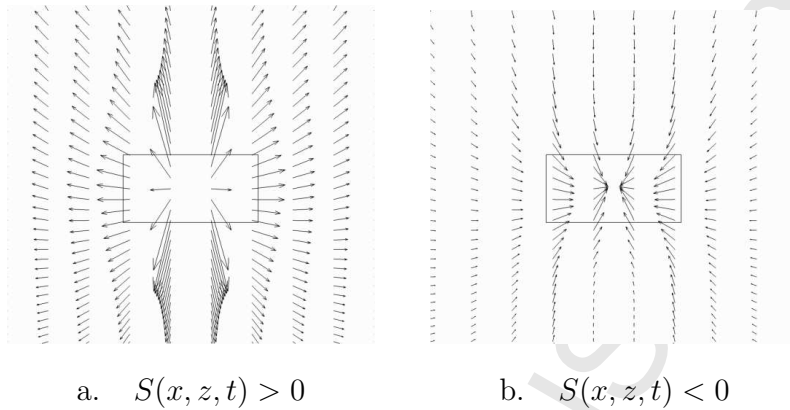


Figure 6: Velocity fields generated by the presence of the source function.

The two wave trains propagate in opposite directions towards both ends of the numerical domain. The Neumann boundary condition is thus set at the left side of the numerical domain to let the outgoing wave exit the numerical domain. In order to ensure that no numerical reflection occurs at the left side of the numerical domain, a sponge layer is set in addition to the Neumann boundary condition. It consists in a region where the permeability coefficient K is chosen such that the outgoing wave train is properly attenuated before reaching the open boundary.

As detailed by Hieu and Tanimoto [20], the source function is gradually intensified during the first four wave periods to ensure a stable regular wave train generation. So the first four generated waves are smaller than the experimental wave height. The small waves are observed to reach the shore and run-up along the beach without breaking. After four wave periods, the simulated waves reach the desired amplitude and the sixth wave starts breaking as a plunging breaker at $x_b \simeq 108 \text{ cm}$ away from the shoreline. The

1
2
3
4
5
6
7
8
9 breaking point then moves offshore, as the next two waves overturn as strong
10 plunging breakers again. The first spilling event is observed as the ninth
11 wave break. Fifteen breaking waves were simulated. Only instantaneous
12 quantities are presented and discussed.
13
14
15
16

17 *3.3. Results and discussion*

18
19 Experimentally, the white cap was about 1 – mm thick as shown by
20 Kimmoun and Branger [1] in their Figs. 4 - windows 2 and 3. So, numerically,
21 the mesh grid refinement and the distribution were chosen to be able to
22 capture this feature. In Figs. 7, 8, 10 and 11, we present the free surface
23 evolution with the numerical velocity field in the water, corresponding to
24 the 10th breaking wave. In Figs. 12, we present some snapshots of the free
25 surface evolution with the numerical velocity fields in both media, air and
26 water, corresponding to the same 10th breaking wave.
27
28
29
30
31
32
33
34
35

36 *3.3.1. General flow description*

37
38 Spilling breakers are observed to start as a small zone of bubbles and
39 droplets on the forward side of the crest [59, 1]. This small region then grows
40 by spreading downslope, most of the forward face becoming a turbulent flow
41 region. Duncan [59] reported that, for the long wavelengths considered here,
42 spilling breakers can be initiated by a small jet at the crest of the wave,
43 creating a small turbulent patch of fluid well above the mean water level.
44 Figs. 7 present the initiation of the spilling phase. Once the front face
45 of the crest steepens and becomes vertical (Fig. 7 a), a thin jet of water
46 is indeed observed to be projected (Fig. 7 b). In our numerical results,
47 the spilling phase then starts as a very weak plunging breaking wave, with a
48
49
50
51
52
53
54
55
56
57
58
59
60
61
62
63
64
65

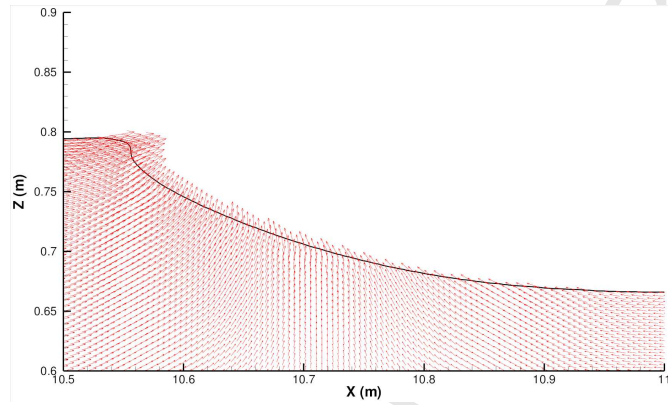
1
2
3
4
5
6
7
8
9
10
11
12
13
14
15
16
17
18
19
20
21
22
23
24
25
26
27
28
29
30
31
32
33
34
35
36
37
38
39
40
41
42
43
44
45
46
47
48
49
50
51
52
53
54
55
56
57
58
59
60
61
62
63
64
65

small tongue of water thrown from the crest developing and free-falling down forward into a characteristic overturning motion. This is in accordance with reports from Duncan [59] and Kimmoun and Branger [1]. Miller [10] also presented pictures showing a spilling breaking wave starting with a $5 - mm$ high impinging jet at the crest of the wave. Once the jet is ejected from the wave crest and plunges down, it hits the water at the plunge point, located very near the crest of the wave. The plunging jet closes over a small gas pocket (Fig. 8 c). The resulting splash is directed down the wave leading to a spilling breaker (Fig. 8 d), where white foam, consisting of a turbulent air/water mixing, should appear at the wave crest and spill down the front face of the propagating wave [59, 1].

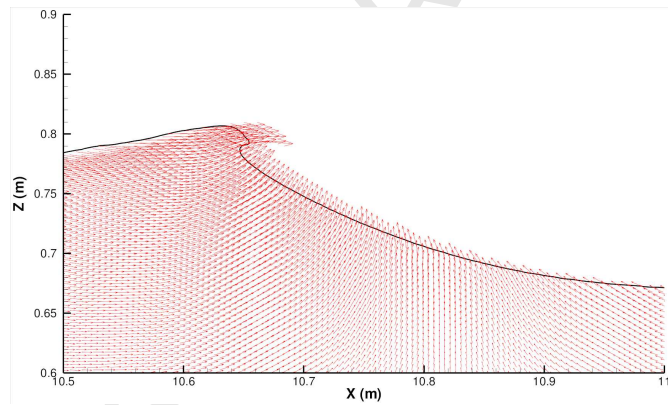
However, compared with the $1 - mm$ thick layer of foam initiating the experimental spilling wave from Kimmoun and Branger [1], we find that the gas pockets entrapped are about $5 - mm$ thick. Fig. 9 presents the jet appearing at the wave crest and the mesh grid density used to capture the generation of the jet. The jet is clearly very small, about $1 - cm$ high, but it is probably thicker than experimentally. This is probably due to the same tendency detailed in section 2.4, where the plunging jet was also thicker than experimentally measured.

Then, the spilling breaker transitions into a strong plunging breaker (Fig. 10 a). A jet is ejected farther towards the lower part of the face of the steepening wave. The plunging breaking wave is then responsible for the generation of larger jet-splash cycles, this, in turn, being responsible for the generation of a sequence of large-scale coherent vortices (Fig. 10 b).

A high velocity region is located at the breaking crest of the wave. High

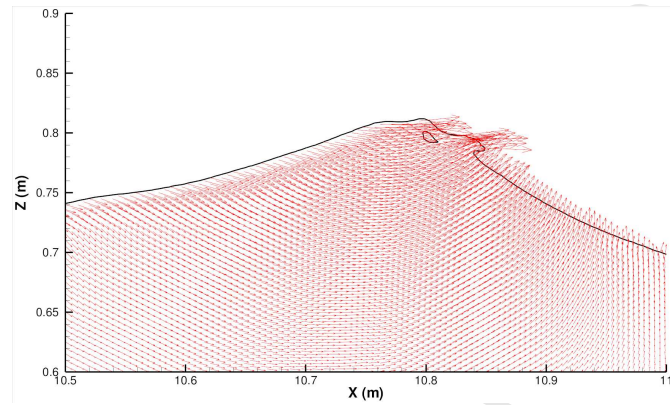


(a)

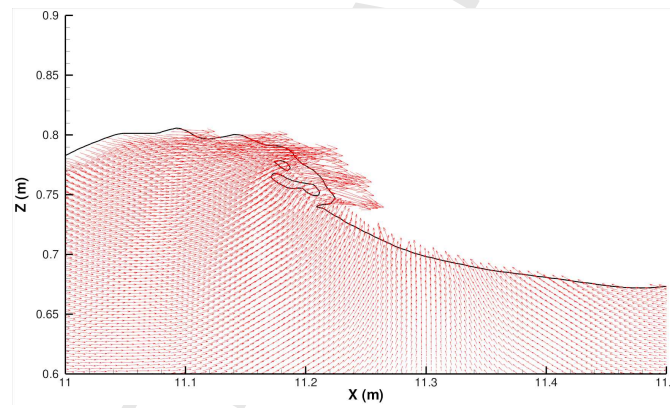


(b)

Figure 7: Breaking wave evolution with velocity field in water. Only one vector over two is shown. Tenth breaking wave spilling phase initiation and jet ejection. The free surface profile corresponds to $C = 0.5$.



(c)



(d)

Figure 8: Breaking wave evolution with velocity field in water. Only one vector over two is shown. Tenth breaking wave spilling phase initiation and air entrainment (continuation of Figs. 7). The free surface profile corresponds to $C = 0.5$.

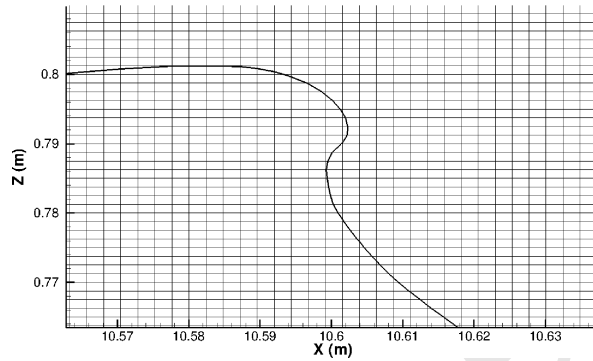


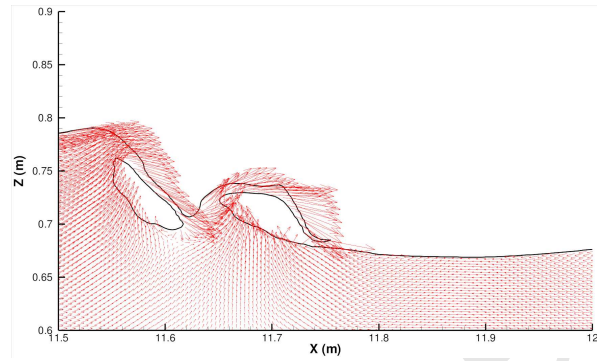
Figure 9: Jet ejection at the crest of the breaking wave for initiation of the spilling phase. Mesh grid is shown with the free surface profile corresponding to $C = 0.5$. Dual grid not shown here.

splash-ups are rising, with high velocities directed upward, in the wave propagation direction, which generates counter- and co-rotative vortices (Figs. 10 b and c), as observed by Bonmarin [60], Miller [10] or Sakai et al. [61]. This process is observed to repeat, each successive splash-up being weaker than the preceding one. Large volumes of air and water are put into rotation, the successive rebounds causing more entrainment of air and energy dissipation. Miller [10] indicated the formation of many air bubbles during the jet-splash cycles which illustrated that the vortices in plunging breakers significantly affect bottom flow. Large spinning gas pockets are observed in our numerical results, dissipating wave energy. Most of the rotating structures are entrained to the bottom before rising again to the surface. And once the wave moves into a bore propagating towards the shoreline (Figs. 11 d to f), we have very similar results for the free surface description detailed by Kimmoun and Branger [1]. High velocities are located near the free surface,

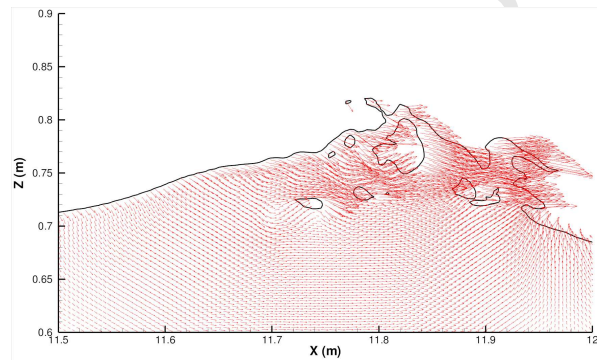
1
2
3
4
5
6
7
8
9 due the jet-splash cycles, during the bore propagation. The free surface is
10 distorted and very dynamic. The bore running up the beach at some point
11 meets the flow running down from the previous broken wave.
12
13

14
15 Nevertheless, discrepancies again appear. Experimentally, air cavities are
16 observed to be quickly fragmented into large plumes of bubbles. The dislo-
17 cation of the gas pockets into small bubbles cannot be simulated, even if, in
18 the numerical results, the gas pockets correspond to some air-water mixing
19 zones observed in the experimental pictures. This is due to the mesh grid
20 resolution, which is still too coarse to be able to capture this flow feature.
21 Indeed, the order of magnitude of bubble radii is usually $10^{-4} m$ [62], whereas
22 our mesh grid resolution is $\Delta x_{min} \simeq 5 \cdot 10^{-4} m$ and $\Delta z_{min} \simeq 1.25 \times 10^{-3} m$
23 thanks to the dual grid. We are able to track the largest gas pockets and
24 bubbles greater than $1 mm$, as illustrated in the figures presented in this
25 paper, where a large variety of inclusion length scales can be seen. Turbu-
26 lence is associated with air entrainment, which is responsible for wave energy
27 damping in the surf zone. In the experiments, it appears that the entrained
28 air bubbles are contained mostly in the large structures and diffused towards
29 the bottom due to the eddies. The rate of energy dissipation is increased
30 with the bubble penetration depth and strong vertical motion is induced
31 by the rising air bubbles. These mechanisms are mostly 3D, which cannot
32 be taken into account in a 2D numerical simulation. Moreover, numerical
33 diffusion due to the LW-TVD method [46] must also be responsible for the
34 discrepancies. The free surface is diffused over three mesh grid cells, so any
35 small inclusions (droplets or bubbles) are described less precisely.
36
37
38
39
40
41
42
43
44
45
46
47
48
49
50
51
52
53
54

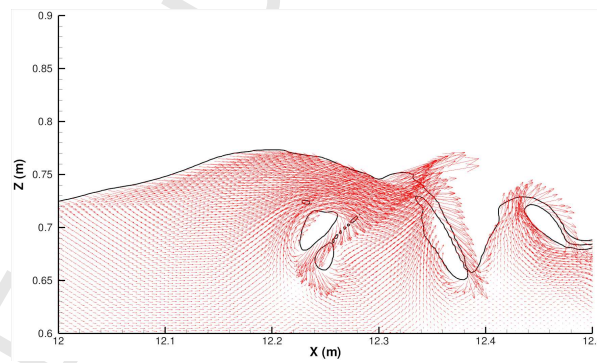
55 We can also see strong flow dynamics in the air. We can see that the
56
57
58



(a)



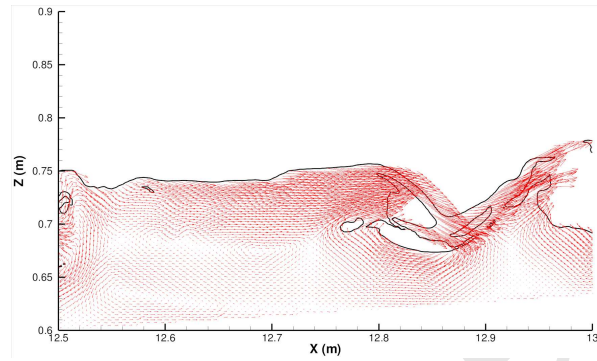
(b)



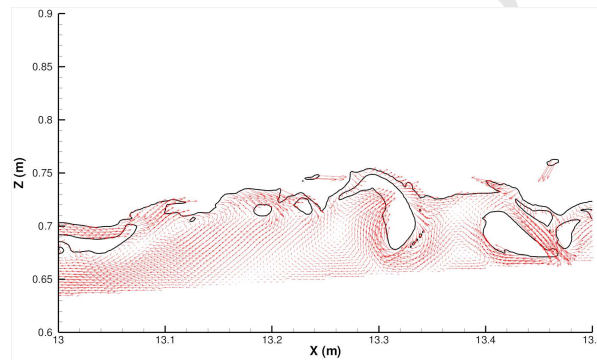
(c)

Figure 10: Wave in the process of breaking with velocity field in water. Only one vector over two is shown. Tenth breaking wave transition to strong plunging breaker with splash-ups generation and air entrainment (continuation of Figs. 7 and 8). The free surface profile corresponds to

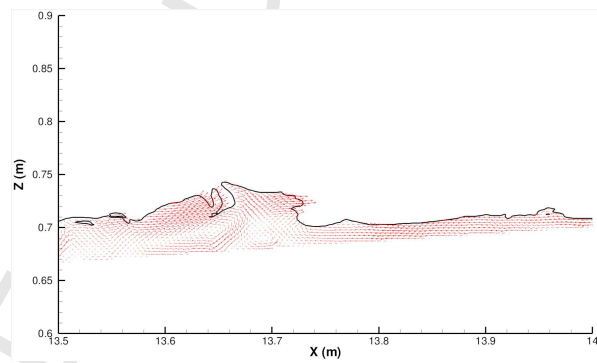
$$C = 0.5.$$



(d)



(e)



(f)

Figure 11: Wave in the process of breaking with velocity field in water.

Only one vector over two is shown. Tenth breaking wave transition to strong plunging breaker and run-up of the bore (continuation of Figs. 7, 8 and 10). The free surface profile corresponds to $C = 0.5$.

1
2
3
4
5
6
7
8
9
10
11
12
13
14
15
16
17
18
19
20
21
22
23
24
25
26
27
28
29
30
31
32
33
34
35
36
37
38
39
40
41
42
43
44
45
46
47
48
49
50
51
52
53
54
55
56
57
58
59
60
61
62
63
64
65

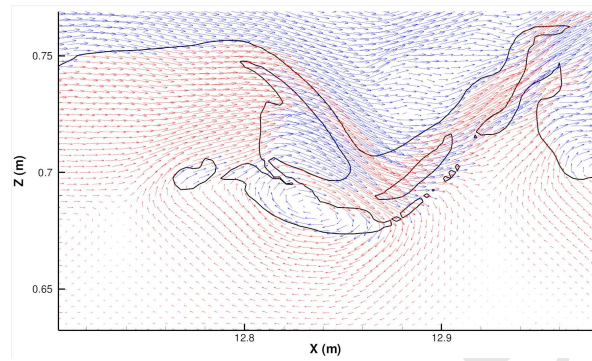
1
2
3
4
5
6
7
8
9
10
11
12
13
14
15
16
17
18
19
20
21
22
23
24
25
26
27
28
29
30
31
32
33
34
35
36
37
38
39
40
41
42
43
44
45
46
47
48
49
50
51
52
53
54
55
56
57
58
59
60
61
62
63
64
65

spilling phase occurs in quiet air dynamics and then meets air agitation generated by the previous breaking waves. A large amount of air is affected by the violence of the plunging breaking event. Figs 12 present some snapshots of gas pockets entrapped at various stages of the breaking of the tenth wave. Rotating and fractioning air pockets can be clearly seen. A large range of inclusions can be described by the numerical simulation, interacting with complex free surface behavior and chaotic hydrodynamics.

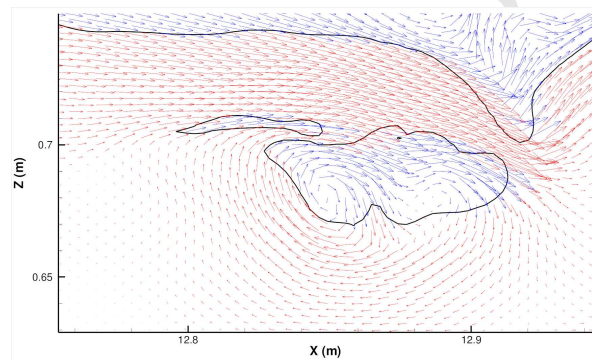
3.3.2. Quantitative comparisons

Table 3 compares the locations of the spilling breaking point, the plunging occurrence and the first splash-up generation, from the numerical and experimental results. The shoreline is located at $x_S = 14.075 \text{ m}$ (see Fig. 5). The wave height at breaking is $H_b = 13 \text{ cm}$, compared with the experimental value $H_b = 14 \text{ cm}$. The numerical breaking point is located at $x_b \simeq 358 \text{ cm}$ away from the shoreline, compared with the experimental value $x_b \simeq 250 \text{ cm}$. The occurrence of breaking was numerically detected when the horizontal velocity component reached a magnitude higher than the wave celerity, matching with a vertical topography of the front face of the wave (see Fig. 10 a). The sequence of the main events can be qualitatively well described by the numerical tool, as the same distance separates approximately each event.

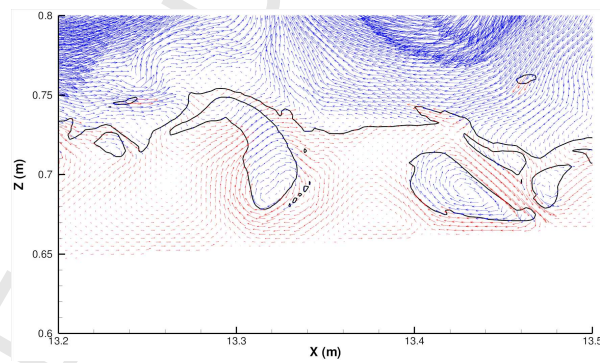
Figure 13 compares the numerical and experimental results for the crest-envelopes (locations of the wave maxima) and the trough-envelopes (locations of the wave minima). Arrows indicate the locations of the main events (beginning of breaking, beginning of plunging and beginning of the first splash-up). The general trend of the flow is found to be qualitatively well described.



(a)



(b)



(c)

Figure 12: Snapshots of the wave in the process of breaking with velocity field in air and water. Only one vector over two is shown. Tenth breaking wave transition to strong plunging breaker with rotating and dislocating gas pockets. The free surface profile corresponds to $C = 0.5$.

1
2
3
4
5
6
7
8
9
10
11
12
13
14
15
16
17
18
19
20
21
22
23
24
25
26
27
28
29
30
31
32
33
34
35
36
37
38
39
40
41
42
43
44
45
46
47
48
49
50
51
52
53
54
55
56
57
58
59
60
61
62
63
64
65

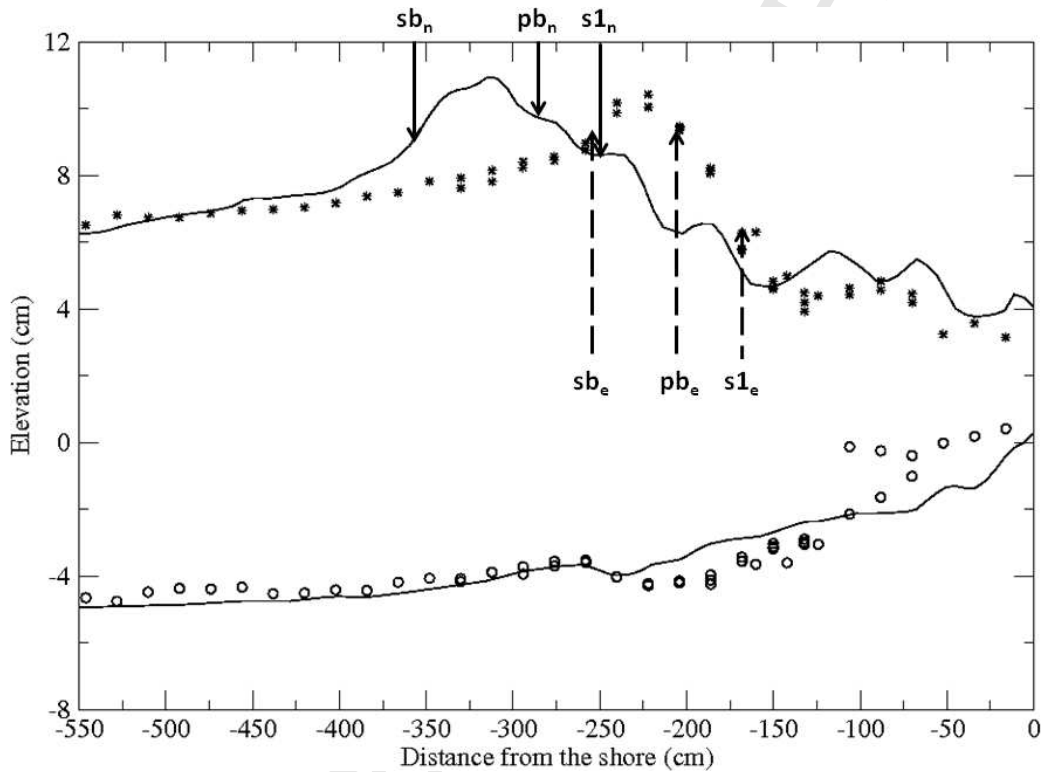


Figure 13: Comparison of the space evolution of the maximum and minimum water levels near the shoreline. Symbols: experimental measurements (stars: wave crest; circles: wave trough). Solid lines: numerical results. The occurrence of the main events are indicated, for the numerical (sb_n , pb_n and $s1_n$) and experimental results (sb_e , pb_e and $s1_e$).

	Experimental study	Numerical simulation
$H_b(cm)$	14	13
$sb(cm)$	$\simeq -250$	$\simeq -358$
$pb(cm)$	$\simeq -210$	$\simeq -280$
$s1(cm)$	$\simeq -170$	$\simeq -250$

Table 3: Experimental and numerical values for the approximate locations of the beginning of the main events: beginning of spilling breaking sb , beginning of plunging breaking pb and beginning of first splash-up $s1$ (see Figs. 12 and 13 from Kimmoun and Branger [1]). Distances are given from the shore.

Figure 14 compares the numerical and experimental wave profiles and velocity fields for the main events. Despite the discrepancies in the abscissae, a general agreement can be seen in the velocity magnitudes and free surface description. Figure 15 presents the numerical and experimental wave profiles when the broken wave runs-up along the beach. Air entrainment can be seen in the experimental pictures with the gray areas. As already mentioned, the gas pockets observed in the numerical pictures correspond to some air-water mixing zones presented in the experimental pictures, but the coarse mesh grid size does not allow the dislocation of the pockets into bubbles. Splash-ups cycles are well described, with horizontal eddies generation [21, 1].

The general trend of the flow dynamics is found to be correctly simulated.

3.3.3. General discussion

So, we slightly underpredict the wave height at breaking and waves break earlier than experimentally observed. It has been observed that a steady

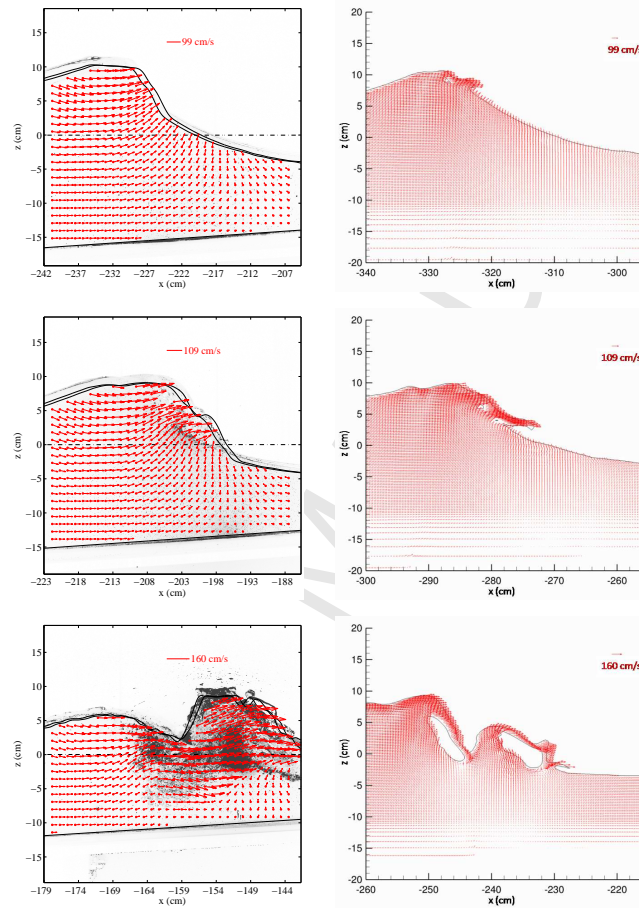


Figure 14: Comparison for the main breaking events (spilling sb , plunging pb and first splash-up $s1$). Right column: numerical results; left column: experiments.

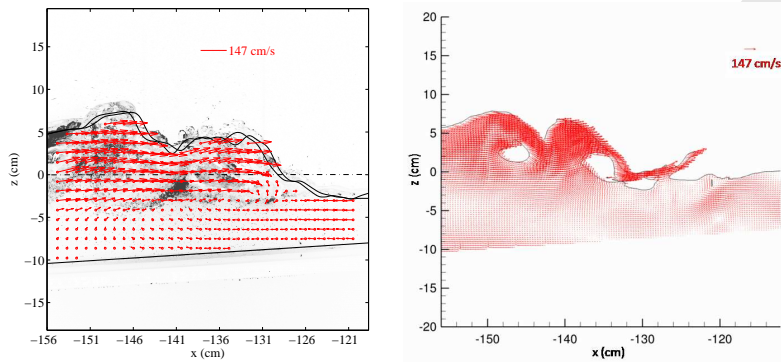


Figure 15: Comparison for the broken wave running-up the beach. Right column: numerical results; left column: experiments.

breaking point was not yet reached. Indeed, some variations occurred in the last breaking waves giving x_b varying ± 60 cm. This is consistent with the experimental observations, the breaking point varying by ± 30 cm around the average value. For each experimental run, the 128 first wave cycles were dedicated to reaching a statistical quasi-stationary sea-state before starting data acquisition [1]. Image acquisition duration was set to 128 wave periods (wave-cycles 129 to 256). Experimentally, the ten first breaking waves were observed to differ from one another.

This remark raises an issue that should be addressed: how many wave cycles should be simulated to be compared with experimental results? For example, Ting and Kirby [63, 64, 65] indicated that waves were generated for a minimum of 20 mn before data were taken, which gives 250 to 600 periodic waves (considering plunging and spilling breakers, respectively). Lin and Liu [66] simulated about ten periodic waves considering spilling breakers [64]. The computed results for mean velocities and free surface profiles

1
2
3
4
5
6
7
8
9 indicated that the waves computed in the surf zone have nearly, but not com-
10 pletely, reached the quasi-steady state, *i.e.* there was very a small difference
11 between two successive wave cycles. Lin and Liu [67] confirmed that, with
12 the improvement of the wave generation mechanism and absorbing bound-
13 ary conditions, the RANS models could run a long time until the waves
14 reached the quasi-steady state, during which both the mean water level and
15 time-averaged mean flow field could be accurately computed. However, the
16 turbulence closure models did not give completely satisfactory results for tur-
17 bulence simulation in the surf zone, the errors ranging from 25% to 100% for
18 the turbulence calculation in the spilling breaker. With LES, Christensen [9]
19 computed the experimental configurations of Ting and Kirby [64, 65], calcu-
20 lating average quantities over the last five wave periods considering 16 to 20
21 wave periods (plunging and spilling breakers, respectively). Wang et al. [23]
22 simulated up to ten spilling waves [64], calculating average quantities over
23 the last two wave periods. Hieu and Tanimoto [20] set a computation time
24 of 50 s, checking that time profiles of free surface elevations were almost sta-
25 ble after 30 s. When compared with to experimental results [64, 65], better
26 agreement was shown for plunging breakers. Nadoaka et al. [68] discussed
27 the fact that the breaking point is sensitive to any imperfection in wave
28 generation or to the effect of the previous broken wave. Therefore, the dif-
29 ferent wave generation procedures used between experiments and numerical
30 simulations may also have contributed to the discrepancies observed in the
31 comparisons presented in this paper. High order moments, such as skewness
32 and flatness of the velocity signal, probably have to be estimated to check
33 that steady state is reached in numerical simulations, to ensure accurate
34
35
36
37
38
39
40
41
42
43
44
45
46
47
48
49
50
51
52
53
54
55
56
57
58
59
60
61
62
63
64
65

1
2
3
4
5
6
7
8
9
10
11
12
13
14
15
16
17
18
19
20
21
22
23
24
25
26
27
28
29
30
31
32
33
34
35
36
37
38
39
40
41
42
43
44
45
46
47
48
49
50
51
52
53
54
55
56
57
58
59
60
61
62
63
64
65

turbulent quantities.

It has therefore been proved that our simulation of fifteen wave periods was insufficient to get a stable and accurate breaking point. Indeed, we observed that the last three waves broke as plunging breakers. So more wave periods would be needed to clearly address this issue. Thus, we did not calculate average quantities, considering the expected discrepancies which could have resulted from the comparisons. Considering these simulations as a validation step, our numerical model gives very satisfactory and encouraging results for this 2D configuration.

4. Conclusions and perspectives

We focused on describing the spilling phase of the experiments detailed by Kimmoun and Branger [1]. The numerical results presented in this paper concern instantaneous quantities, simulating 2D regular waves breaking over a sloping beach. Our model was found to be reliable to describe correctly the complicated two-phase flow interactions that happen when waves break. The breaking process, in terms of wave overturning and splash-up occurrence, is in accordance with the general observations given in the literature. Air entrainment is described, which is important as it plays a great role in the energy dissipation process. The utility of the numerical approach is to provide a complete and accurate description of free surface and velocity evolutions in both air and water media during the breaking of the waves, which must lead to the understanding of the generation processes of energy dissipation and turbulent flow structures. Nevertheless, wave breaking is a 3D two-phase turbulent problem, so the 2D numerical results presented here consisted in a

1
2
3
4
5
6
7
8
9 first attempt.

10
11 A major limitation of our numerical methods has been illustrated in the
12 results presented in this paper. The accuracy of the whole physical process
13 description is closely linked to the mesh grid size. Although LES allows
14 the use of coarser mesh grids to simulate turbulent flows, on the condition
15 that an appropriate subgrid model is implemented, an accurate free surface
16 description requires fine mesh grids. LES of breaking waves involve large
17 numerical domains, to include the generation of regular waves propagating
18 towards sloping beaches, and fine mesh grid resolutions to be able to describe
19 a large variety of physical processes (overturning jet, air entrainment, gas
20 pocket dislocations and coalescences). Long CPU time for the calculations
21 is also required to simulate a sufficient number of wave periods to reach a
22 steady state in the surf zone to perform correct averaging over time. Parallel
23 computing will enhance access to a better level of description of the turbulent
24 behavior of the entrained and rising air bubbles, providing refined mesh grids
25 are used to ensure an accurate free surface description [36].

26
27
28
29
30
31
32
33
34
35
36
37
38
39
40 With mesh refinement and 3D simulations, we could expect a better de-
41 scription of the air entrainment and energy dissipation. Considering the
42 difficulty to capture all the small bubbles and droplets encountered in the
43 wave breaking problem, these small interface structures can also be consid-
44 ered as subgrid interfaces. Mimicking the LES approach for turbulence, an
45 appropriate model of inclusions smaller than the mesh grid size could then
46 be proposed [69].
47
48
49
50
51
52
53
54
55
56
57
58
59
60
61
62
63
64
65

5. Acknowledgements

The authors wish to thank the Aquitaine Regional Council for the financial support towards a 256-processor cluster investment, located in the TREFLE laboratory. This work was granted access to the HPC resources of CINES under allocation 2009-c2009026104 made by GENCI (Grand Equipement National de Calcul Intensif). The authors would like to acknowledge the financial and scientific support of the French INSU - CNRS (Institut National des Sciences de l'Univers - Centre National de la Recherche Scientifique) program IDAO ("Interactions et Dynamique de l'Atmosphère et de l'Océan"). This work was carried out under the project "Wave-induced circulation in the surf zone" coordinated by Dr. Hervé Michallet (LEGI - Grenoble).

References

- [1] O. Kimmoun, H. Branger, A piv investigation on laboratory surf-zone breaking waves over a sloping beach, *J. Fluid Mech* 588 (2007) 353–397.
- [2] J. A. Battjes, Surf-zone dynamics, *Annu. Rev. Fluid Mech.* 20 (1988) 257–293.
- [3] I. A. Svendsen, U. Putrevu, Surf-zone hydrodynamics, Vol. 2 of *Advances in Coastal and Ocean Eng.*, World Scientific, 1996, pp. 1–78.
- [4] Q. Zhao, K. Tanimoto, Numerical simulation of breaking waves by large eddy simulation and vof method, in: *Proc. of the 26th Int. Conf. Coastal Eng.*, Vol. 1, ASCE, 1998, pp. 892–905.

- 1
2
3
4
5
6
7
8
9 [5] E. D. Christensen, R. Deigaard, Large eddy simulation of breaking
10 waves, *Coastal Eng.* 42 (2001) 53–86.
11
12
13 [6] P. D. Hieu, K. Tanimoto, V. T. Ca, Numerical simulation of breaking
14 waves using a two-phase flow model, *Applied Mathematical Modelling*
15 28 (11) (2004) 983–1005.
16
17
18 [7] Q. Zhao, S. Armfield, K. Tanimoto, Numerical simulation of breaking
19 waves by multi-scale turbulence model, *Coastal Eng.* 51 (2004) 53–80.
20
21
22 [8] Y. Watanabe, H. Saeki, R. J. Hosking, Three-dimensional vortex struc-
23 tures under breaking waves, *J. Fluid Mech* 545 (2005) 291–328.
24
25
26 [9] E. D. Christensen, Large eddy simulation of spilling and plunging break-
27 ers, *Coastal Eng.* 53 (2006) 463–485.
28
29
30 [10] R. L. Miller, Role of vortices in surf zone predictions : sedimentation
31 and wave forces, *Soc. Econ. Paleontol. Mineral. Spec. Publ.*, R. A. Davis
32 and R. L. Ethington, 1976, Ch. 24, pp. 92–114.
33
34
35 [11] K. Nadaoka, T. Kondoh, Laboratory measurements of velocity field
36 structure in the surf zone by ldv, *Coastal Eng. J. in Japan* 25 (1982)
37 125–145.
38
39
40 [12] E. Lamarre, W. K. Melville, Air entrainment and dissipation in breaking
41 waves, *Nature* 351 (1991) 469.
42
43
44 [13] H. H. Hwung, J. M. Chyan, Y. C. Chung, Energy dissipation and air
45 bubbles mixing inside surf zone, in: *Proc. 23rd Intl Conf. on Coastal*
46 *Eng.*, 1992, pp. 308–321.
47
48
49
50
51
52
53
54
55
56
57
58
59
60
61
62
63
64
65

- 1
2
3
4
5
6
7
8
9 [14] H. Chanson, S. Aoki, M. Maruyama, Unsteady air bubble entrainment
10 and detrainment at a plunging breaker: dominant time scales and simi-
11 larity of water level variations, *Coastal Eng.* 46 (2002) 139–157.
12
13
14
15 [15] C. Lin, H. H. Hwung, External and internal flow fields of plunging break-
16 ers, *Experiments in Fluids* 12 (1992) 229–237.
17
18 [16] H. Chanson, J.-F. Lee, Plunging jet characteristics of plunging breakers,
19 *Coastal Eng.* 31 (1997) 125–141.
20
21
22 [17] Z.-C. Huang, S.-C. Hsiao, H.-H. Hwung, K.-A. Chang, Turbulence and
23 energy dissipations of surf-zone spilling breakers, *Coastal Eng.* 56 (2009)
24 733–746.
25
26 [18] S. F. Bradford, Progress in the observation and modeling of turbulent
27 multi-phase flows, *Environmental Fluid Mechanics* 9 (2) (2009) 121–123.
28
29 [19] E. D. Christensen, D.-J. Walstra, N. Emerat, Vertical variation of the
30 flow across the surf zone, *Coastal Eng.* 45 (2002) 169–198.
31
32 [20] P. D. Hieu, K. Tanimoto, V. T. Ca, Verification of a vof-based two-
33 phase flow model for wave breaking and wave-structure interactions,
34 *Ocean Engineering* 33 (2006) 1565–1588.
35
36 [21] P. Lubin, S. Vincent, S. Abadie, J.-P. Caltagirone, Three-dimensional
37 large eddy simulation of air entrainment under plunging breaking waves,
38 *Coastal Eng.* 53 (2006) 631–655.
39
40 [22] Z. Wang, J. Yang, B. Koo, F. Stern, A coupled level set and volume-of-
41
42
43
44
45
46
47
48
49
50
51
52
53
54
55
56
57
58
59
60
61
62
63
64
65

- 1
2
3
4
5
6
7
8
9 fluid method for sharp interface simulation of plunging breaking waves,
10 International Journal of Multiphase Flow 35 (3) (2009) 227–246.
11
12
13 [23] Z. Wang, Q. Zou, D. Reeve, Simulation of spilling breaking waves using
14 a two phase flow cfd model, Computers and Fluids 38 (10) (2009) 1995–
15 2005.
16
17
18 [24] A. Iafrati, Numerical study of the effects of the breaking intensity on
19 wave breaking flows, J. Fluid Mech 622 (2009) 371–411.
20
21
22 [25] P. Lubin, H. Branger, O. Kimmoun, Large eddy simulation of regular
23 waves breaking over a sloping beach, in: J. M. Smith (Ed.), Proceedings
24 of the 30st International Conference on Coastal Engineering, Vol. 1,
25 World Scientific, 2006, pp. 238–250. doi:10.1142/9789812709554_0021.
26
27
28 [26] O. Kimmoun, H. Branger, B. Zucchini, Laboratory piv measurements of
29 wave breaking on a beach, in: Proc. 14th Int. Offshore and Polar Engng.
30 Conf., Vol. 3, 2004, pp. 293–298.
31
32
33 [27] I. Kataoka, Local instant formulation of two-phase flow, Int. J. Multi-
34 phase Flow 12 (5) (1986) 745–758.
35
36
37 [28] E. Arquis, J.-P. Caltagirone, Sur les conditions hydrodynamiques au
38 voisinage d’une interface milieu fluide - milieu poreux : application à la
39 convection naturelle, C. R. Acad. Sci. Série II b 299 (1984) 1–4.
40
41
42 [29] P. Angot, C. Bruneau, P. Fabrie, A penalization method to take into ac-
43 count obstacles in incompressible viscous flows, *Numerische Mathematik*
44 81 (4) (1999) 497–520.
45
46
47
48
49
50
51
52
53
54
55
56
57
58
59
60
61
62
63
64
65

- 1
2
3
4
5
6
7
8
9
10 [30] K. Khadra, P. Angot, S. Parneix, J.-P. Caltagirone, Fictitious domain
11 approach for numerical modelling of navier-stokes equations, *Int. J. Nu-*
12 *mer. Meth. Fluids* 34 (2000) 651–684.
13
14
15 [31] P. Lubin, J.-P. Caltagirone, Large eddy simulation of the hydrodynamics
16 generated by breaking waves, in: Q. Ma (Ed.), *Advances in numerical*
17 *simulation of nonlinear water waves*, Vol. 11 of *Advances in Coastal and*
18 *Ocean Engineering*, World Scientific Publishing Company, 2010, Ch. 16,
19 pp. 575–604.
20
21
22 [32] P. Sagaut, *Large Eddy Simulation for incompressible flows - An intro-*
23 *duction*, Springer Verlag, 1998.
24
25
26 [33] P. Lubin, Large eddy simulation of plunging breaking waves, Ph.D. the-
27 sis, Université Bordeaux I, in English (2004).
28
29
30 [34] P. Helluy, F. Gollay, S. T. Grilli, N. Seguin, P. Lubin, J.-P. Caltag-
31 girone, S. Vincent, D. Drevard, R. Marcer, Numerical simulations of
32 wave breaking, *Mathematical Modelling and Numerical Analysis* 39 (3)
33 (2005) 591–608.
34
35
36 [35] P. Lubin, S. Glockner, H. Chanson, Numerical simulation of a weak
37 breaking tidal bore, *Mechanics Research Communications* 37 (1) (2010)
38 119–121.
39
40
41 [36] P. Lubin, H. Chanson, S. Glockner, Large eddy simulation of turbulence
42 generated by a weak breaking tidal bore, *Environmental Fluid Mechan-*
43 *ics* 10 (5) (2010) 587–602.
44
45
46
47
48
49
50
51
52
53
54
55
56
57
58
59
60
61
62
63
64
65

- 1
2
3
4
5
6
7
8
9 [37] P. Sagaut, R. Grohens, Discrete filters for large eddy simulation, *Int. J.*
10 *Numer. Meth. Fluids* 31 (1999) 1195–1220.
11
12
13 [38] M. Rudman, A volume-tracking method for incompressible multifluid
14 flows with large density variations, *Int. J. Numer. Meth. Fluids* 28 (2)
15 (1998) 357–378.
16
17
18 [39] M. Fortin, R. Glowinski, Méthodes de lagrangien augmenté. Application
19 à la résolution numérique de problèmes aux limites, Dunod, Paris, 1982.
20
21
22 [40] H. Uzawa, Iterative method for concave programming, K. J. Arrow, L.
23 Hurwicz and H. Uzawa, editors, *Studies in linear and Nonlinear Pro-*
24 *gramming*, Stanford University Press, Stanford, CA, 1958.
25
26
27 [41] S. Vincent, J.-P. Caltagirone, P. Lubin, T. N. Randrianarivelo, An
28 adaptative augmented lagrangian method for three-dimensional multi-
29 material flows, *Computers and Fluids* 33 (2004) 1273–1289.
30
31
32 [42] S. V. Patankar, *Numerical heat transfer and fluid flow*, Hemisphere Pub-
33 *lishing Corporation*, New York, 1990.
34
35
36 [43] P. R. Amestoy, I. S. Duff, J. Koster, J.-Y. L'Excellent, A fully
37 asynchronous multifrontal solver using distributed dynamic scheduling,
38 *SIAM Journal on Matrix Analysis and Applications* 23 (1) (2001) 15–41.
39
40
41 [44] P. R. Amestoy, A. Guermouche, J.-Y. L'Excellent, S. Pralet, Hybrid
42 scheduling for the parallel solution of linear systems, *Parallel Computing*
43 32 (2) (2006) 136–156.
44
45
46
47
48
49
50
51
52
53
54
55
56
57
58
59
60
61
62
63
64
65

- 1
2
3
4
5
6
7
8
9 [45] P. Lin, P. L.-F. Liu, Free surface tracking methods and their applications
10 to wave hydrodynamics, Vol. 5 of *Advances in Coastal and Ocean Eng.*,
11 World Scientific, 1999, pp. 213–240.
12
13
14
15 [46] R. J. LeVeque, *Numerical methods for conservation laws*, Lectures in
16 Mathematics, Birkhauser, Zurich, 1992.
17
18
19 [47] P. Lubin, S. Vincent, J.-P. Caltagirone, On the navier-stokes equations
20 simulation of the head-on collision between two surface solitary waves,
21 C. R. Mécanique 333 (4) (2005) 351–357.
22
23
24
25 [48] P. Lin, P. L.-F. Liu, Internal wave-maker for navier-stokes equations
26 models, *J. of Waterway, Port, Coastal, and Ocean Eng.* 125 (4) (1999)
27 207–215.
28
29
30
31 [49] T. Yasuda, H. Mutsuda, N. Mizutani, Kinematics of overturning solitary
32 waves and their relations to breaker types, *Coastal Eng.* 29 (1997) 317–
33 346.
34
35
36
37 [50] J.-J. Lee, J. E. Skjelbreia, F. Raichlen, Measurements of velocities in soli-
38 tary waves, *J. of Waterway, Port, Coastal, and Ocean Eng.* WW2 (108)
39 (1982) 200–218.
40
41
42
43 [51] P. Lubin, H. Lemonnier, Propagation of solitary waves in constant
44 depths over horizontal beds, *Multiphase Science and Technology* 16 (1-3)
45 (2004) 237–248. doi:10.1615/MultScienTechn.v16.i1-3.310.
46
47
48
49 [52] F. J. Seabra-Santos, D. P. Renouard, A. M. Temperville, Numerical and
50 experimental study of the transformation of a solitary wave over a shelf
51 or isolated obstacle, *J. Fluid Mech* 176 (1997) 117–134.
52
53
54
55
56
57
58
59
60
61
62
63
64
65

- 1
2
3
4
5
6
7
8
9 [53] P. L.-F. Liu, Y. Cheng, A numerical study of the evolution of a solitary
10 wave over a shelf, *Phys. Fluids* 13 (6) (2001) 1660–1667.
11
12
13 [54] G. Chen, C. Kharif, S. Zaleski, J. J. Li, Two-dimensional navier-stokes
14 simulation of breaking waves, *Phys. Fluids* 11 (1999) 121–133.
15
16
17 [55] J. D. Fenton, A fifth-order stokes theory for steady waves, *J. of Water-*
18 *way, Port, Coastal, and Ocean Eng.* 111 (1985) 216–234.
19
20
21
22 [56] D. H. Peregrine, Breaking waves on beaches, *Annu. Rev. Fluid Mech.*
23 15 (1983) 149–178.
24
25
26 [57] R. J. Sobey, P. Goodwin, R. J. Thieke, R. J. Westberg, Application of
27 stokes, cnoidal, and fourier wave theories, *J. of Waterway, Port, Coastal,*
28 *and Ocean Eng.* 113 (6) (1987) 565–587.
29
30
31
32 [58] J. D. Fenton, W. D. McKee, On calculating the lengths of water waves
33 14 (1990) 499–513.
34
35
36 [59] J. H. Duncan, Spilling breakers, *Annu. Rev. Fluid Mech.* 33 (2001) 519–
37 547.
38
39
40
41 [60] P. Bonmarin, Geometric properties of deep-water breaking waves, *J.*
42 *Fluid Mech* 209 (1989) 405–433.
43
44
45 [61] T. Sakai, T. Mizutani, H. Tanaka, Y. Tada, Vortex formation in plunging
46 breaker, in: *Proc. ICCE*, 1986, pp. 711–723.
47
48
49 [62] G. B. Deane, M. D. Stokes, Scale dependence of bubble creation mech-
50 anisms in breaking waves, *Nature* 418 (2002) 839–844.
51
52
53
54
55
56
57
58
59
60
61
62
63
64
65

- 1
2
3
4
5
6
7
8
9 [63] F. C. K. Ting, J. T. Kirby, Observation of undertow and turbulence in
10 a laboratory surf zone, *Coastal Eng.* 24 (1994) 51–80.
11
12
13 [64] F. C. K. Ting, J. T. Kirby, Dynamics of surf-zone turbulence in a strong
14 plunging breaker, *Coastal Eng.* 24 (1995) 177–204.
15
16
17 [65] F. C. K. Ting, J. T. Kirby, Dynamics of surf-zone turbulence in a spilling
18 breaker, *Coastal Eng.* 27 (1996) 131–160.
19
20
21
22 [66] P. Lin, P. L.-F. Liu, A numerical study of breaking waves in the surf
23 zone, *J. Fluid Mech* 359 (1998) 239–264.
24
25
26 [67] P. Lin, P. L.-F. Liu, Discussion of vertical variation of the flow across
27 the surf zone, *Coastal Eng.* 50 (3) (2004) 161–164.
28
29
30
31 [68] K. Nadaoka, M. Hino, Y. Koyano, Structure of the turbulent flow field
32 under breaking waves in the surf zone, *J. Fluid Mech* 204 (1989) 359–
33 387.
34
35
36 [69] F. Shi, J. T. Kirby, G. Ma, Modeling quiescent phase transport of air
37 bubbles induced by breaking waves, *Ocean Modelling* 35 (1-2) (2010)
38 105–117.
39
40
41
42
43
44
45
46
47
48
49
50
51
52
53
54
55
56
57
58
59
60
61
62
63
64
65